



Computational fluid dynamics modelling of the regular wave flow regime in air-water downwards annular flows

Nicolò Varallo ^{a,*}, Riccardo Mereu ^a, Giorgio Besagni ^a, Christos N. Markides ^b

^a Politecnico di Milano, Department of Energy, Via Lambruschini 4a, 20156 Milano, Italy

^b Clean Energy Processes (CEP) Laboratory, Department of Chemical Engineering, Imperial College London, South Kensington Campus, London SW7 2AZ, UK

ARTICLE INFO

Keywords:

CFD simulations
Downwards annular flow
Film thickness
Waves
Volume of fluid

ABSTRACT

Although the global flow characteristics of annular gas-liquid flows have been studied experimentally for more than 50 years, the spatiotemporally-resolved details of these flows have remained relatively unexplored until recently, with data provided via advanced experimental methods based, e.g., on optical techniques. Similarly, the numerical modelling of annular flows is still an immature process. The present work aims to provide a computational fluid dynamics (CFD) model based on the volume of fluid (VOF) method for simulating annular gas-liquid flows, setting the stage for a deeper investigation of these flows at global and local scales. The work focuses on the most common downwards annular flow (DAF) flow pattern: the regular wave regime. 3-D and 2-D axisymmetric transient simulations have been performed using a commercial code (ANSYS Fluent 2021 R1). The code is validated through available experimental data regarding topological flow properties, mainly film thickness and wave statistics. The validation results suggest that 3-D simulations are needed to provide predictions that agree with the experimental data, highlighting strong 3-D features in the flow.

1. Introduction

Two-phase gas-liquid annular flows are observed in a broad range of industrial processes, such as production and pipeline systems for oil and gas distribution, steam generators, boiling water reactors, and emergency core cooling facilities for the protection of nuclear reactors (Zabaras et al., 1986; Liu et al., 2021; Zhu et al., 2021).

The annular flow regime is characterised by a central gas core that pushes the liquid into a film flowing on the pipe wall (Wu et al., 2017). Interfacial waves appear along the streamwise direction due to the shear generated by the gas, as seen in Fig. 1. Additionally, gas bubbles are entrained in the liquid film and liquid droplets in the gas core (Schubring et al., 2010).

Two main classes of waves (disturbance and ripple waves) are usually identified and used to differentiate several flow patterns (Webb, Hewitt, 1975). Disturbance waves are the most relevant in practical applications, as they dominate the wave interface. These waves are characterized by a large amplitude, up to 5 times the mean film thickness, and they propagate quickly, generating small-scale ripple waves at their rear slopes (Alekseenko et al., 2008). Ripple waves are smaller disturbances of the flow, associated with low amplitudes, wavelengths,

and short lifetimes (Zadrazil et al., 2014).

Four flow patterns can be differentiated in downwards annular flow (DAF) (Fig. 2): the "dual-wave" regime, where two different disturbance wave types coexist, the "thick-ripple" regime, where a pattern of ripples occupies the interface, the "disturbance wave" regime, characterized by an irregular appearance of large waves along the film substrate that is covered with ripples, and the "regular wave" regime present at high gas velocities and associated with short waves of large amplitude that appear regularly (Zadrazil et al., 2014; Voulgaropoulos et al., 2021).

The flow regimes present in DAF appear due to the flow conditions, orientation and size of the domain, and fluids considered (Voulgaropoulos et al., 2021). Disturbance and ripple waves appear at different frequencies when changing these variables. Gas and liquid entrainment occur along the moving interface and influence the amount of liquid carried by the liquid film and the waves.

Numerical methods have gained popularity in the study of multiphase flows since CFD simulations allow the acquisition of any flow variable at every cell inside the computational domain. The simulation can yield more information as instantaneous, detailed and localized findings are available.

The modelling of annular flow is still challenging due to the significant number of complex mechanisms appearing at the gas-liquid

* Corresponding author.

E-mail address: nicolo.varallo@polimi.it (N. Varallo).

Nomenclature	
Acronyms	
CAP	Capacitance probe method
CFD	Computational fluid dynamics
CFL	Courant Friedrichs Lewy number
CSF	Continuous surface force
DAF	Downwards annular flow
DFT	Discrete Fourier transform
EWF	Enhanced wall functions
FEP	Fluorinated ethylene propylene
FFT	Fast Fourier transform
NITA	Non-iterative time advancement
PDF	Probability density function
PLIF	Planar laser-induced fluorescence
PSD	Power spectral density
RNG	Renormalization group
S-PLIF	Structured planar laser-induced fluorescence
SST	Shear stress transport
VOF	Volume of fluid
Symbols	
α	Volume fraction, [-]
δ	Film thickness, [m]
ε	Turbulent dissipation rate, [$\text{m}^2 \text{s}^{-3}$]
ρ	Density, [kg m^{-3}]
σ_δ	Film roughness, [m]
σ_{GL}	Gas-liquid surface tension, [N m^{-1}]
$\bar{\tau}$	Molecular stresses, [Pa]
$\bar{\tau}_t$	Reynolds stresses, [Pa]
ω	Specific dissipation rate, [s^{-1}]
a	Parameter in the frequency decay function, [Hz]
b	Parameter in the frequency decay function, [Hz/m]
D	Diameter of the pipe, [m]
F	Volumetric force, [N]
f	Frequency, [Hz]
g	Gravity acceleration, [m s^{-2}]
h	Height of the film from the wall, [m]
k	Turbulent kinetic energy, [$\text{m}^2 \text{s}^{-2}$]
L	Length of the pipe, [m]
N	Number of observations, [-]
N_p	Number measurement angles, [-]
N_t	Number of time measurements, [-]
P	Pressure, [Pa]
Re	Reynolds number, [-]
R_{pipe}	Radius of the pipe, [m]
$R_{\text{interface}}$	Distance between gas-liquid interface and pipe axis, [m]
t	Time, [s]
v	Velocity, [m s^{-1}]
z	Axial length, [m]
Subscripts	
∞	Fully developed flow
base	Base film
G	Gas phase
L	Liquid phase
n	n -th time measurement
p	p -th angular measurement
w	Water
wave	Waves
o	Oil
Signal spectral analysis	
M	Hamming window length
S_{xx}	Spectral density
ω_H	Hamming window
$X(k)$	Discrete frequency spectrum
$x(n)$	Time sequence

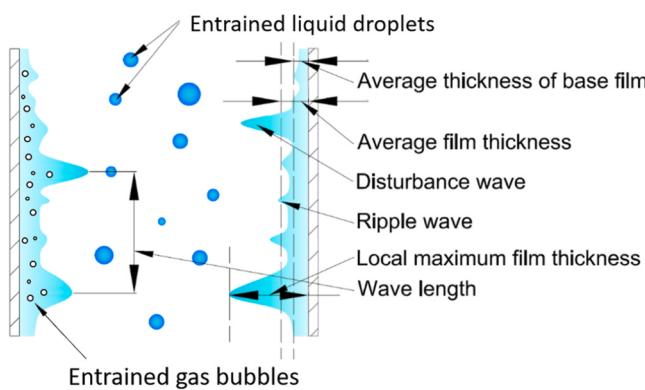


Fig. 1. Key features of gas-liquid annular flow (Xue et al., 2022).

interface.

Jayanti, Hewitt, 1997 were among the first to simulate a physical-defined wave in a two-dimensional domain with periodic boundary conditions. A similar approach was followed by Han, Gabriel, 2006, although more recent research found that annular flow does not present a periodic behaviour. The investigations collected in Table 1 range from 2007 to 2022, and although there are still some 2-D approaches, 3-D models are usually preferred. It is sometimes stated that a 2-D domain cannot correctly describe the droplets dynamic and the liquid film. However, the modelling of a two-dimensional domain

contributes to the reduction of computational requirements.

The VOF model is employed in all the studies, while turbulence modelling is divided between the RNG $k - \varepsilon$ and the SST $k - \omega$ models. The two phases simulated are usually air-water, oil-water, or air-oil, as they are more present in industrial processes. Transient simulations are preferred, with time steps between 1 ms down to 1 ns, except for Riviera et al. (2022), where a steady state simulation is performed to focus on the study of the mean film thickness. Meshing size usually decreases towards the wall to capture the liquid film behaviour well. Boundary conditions usually introduce the liquid and the gas from separate inlets so that the liquid film is formed from the inlet of the pipe. Pressure-outlet and non-slip condition are the most common boundary conditions, and the flow is initialized with the pipe filled by one of the phases.

Considering the gaps in the current numerical modelling of annular flows, this work aims to develop a CFD model that can describe the gas-liquid interactions in annular flows, focusing on the regular wave flow regime.

This paper is organized as follows. Section 2 describes the experimental benchmark used for the model validation, and Section 3 describes the numerical model. Section 4 collects the post-processing of the local data obtained from the numerical simulation. In Section 5, the results from the numerical simulations are presented and compared with the experimental data. Finally, conclusions are drawn, and avenues for future investigation are proposed.

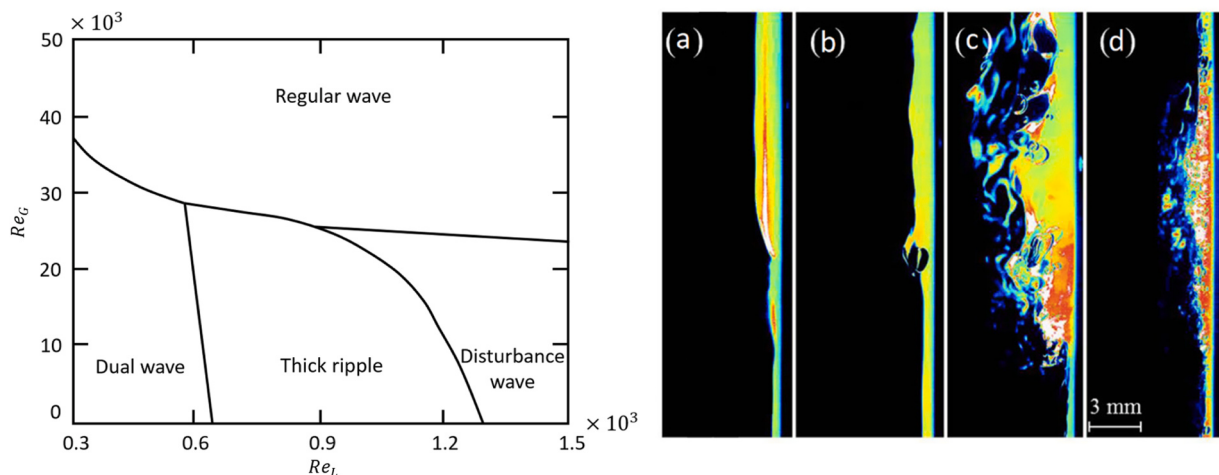


Fig. 2. Flow regime map and instantaneous images of wavefronts for an air-water DAF. (a) “Dual-wave” flow regime, (b) “thick ripple” flow regime, (c) “disturbance wave” flow regime, and (d) “regular wave” flow regime (Voulgaropoulos et al., 2021).

Table 1
Summary of CFD studies of two-phase annular flows in pipes.

Ref.	Flow orientation	Fluids	Operating conditions	Modelling dimension and mesh	Multiphase model	Turbulence model
Han, Gabriel, 2007	Upward	Air - water	$Re_G = 253 - 3037 - 7593$ $Re_L = 1482 - 2328$	2-D	VOF Explicit	RNG $k - \epsilon$ with EWF
De Schepper et al., 2008	Horizontal	Air - water	$Re_G = 182225$ $Re_L = 6540$	3-D	VOF	RNG $k - \epsilon$ with EWF
Ghosh et al., 2010	Downward	Water - oil	$Re_{L,o} = 8.64 - 46.08$ $Re_{L,w} = 14314$	3-D 55 105 cells with local refinement	VOF	RNG $k - \epsilon$ with EWF
Liu et al., 2011	Upward	Air - water	$Re_G = 300 - 3800$ $Re_L = 125000 - 275000$	2-D	VOF with additional eqs.	Standard $k - \epsilon$ with EWF
Fan et al., 2019	Downward	Air - water	$Re_G = 17878$ $Re_L = 350$	3-D 2 920 321 cells with near-wall refinement	VOF with CSF and wall adhesion	SST $k - \omega$ with turbulence damping
Fan et al., 2020	Downwards	Air-water	$Re_L = 140 - 400$ $Re_G = 7800 - 78000$	3D	VOF	SST $k - \omega$ with turbulence damping
Pinilla et al., 2019	Up/downward	Air - oil	Downward: $Re_G = 246 - 24017$ $Re_L = 7.5 - 246$ Upward: $Re_G = 6036 - 99232$ $Re_L = 119 - 6036$	3-D Downward: 153 000 with near-wall refinement Upward: 108 000 with near-wall refinement	VOF	SST $k - \omega$
Wu et al., 2020	90° elbow	Oil - water	$U_{L,o} = 0.31$ [m/s] $U_{L,w} = 0.19$ [m/s]	3-D 240 653 elements	VOF	Standard $k - \epsilon$
Riviera et al., 2022	Downward	Air - water	$Re_G = 0 - 110500$ $Re_L = 800 - 8000$	3-D 600 000 elements with near-wall refinement	VOF	SST $k - \omega$
Angirekula and Gupta, 2022	Horizontal microchannel	Nitrogen dioxide - water	$Re_G = 1600$ $Re_L = 100$	2-D 90 750 elements	VOF	Laminar flow

2. Experimental benchmark

The CFD model validation has been performed by comparing the numerical results with the experimental data from Voulgaropoulos et al. (2021). The experimental flow facility is a 5 m long vertical pipe of 32.4 mm inner diameter (Fig. 3). Different operating conditions were investigated (Fig. 4): the liquid Reynolds number varied between 500 and 1 375, whereas the maximum gas Reynolds number was 137 500, covering all the flow regimes discussed in Section 1.

Air and water are introduced co-currently from the top. Water enters the pipe as a film, through an injector explicitly designed for the facility, allowing the liquid to be injected directly in the axial direction. Two measurement techniques were employed: a non-intrusive optical technique known as planar laser-induced fluorescence (PLIF) and an intrusive method based on capacitance measurements (CAP). Film thickness results were calculated from both methods, while wave statistics were

only obtained from the capacitance probe.

Optical measurements were based on an advanced laser technique known as S-PLIF (Charogiannis et al., 2019; Voulgaropoulos et al., 2021). The water was seeded with a fluorescent dye and was illuminated by a laser sheet from dedicated optics. The scattered light was recorded by a camera that captured images of the flow for 20 s, with a frequency of 100 Hz. The camera was placed at one circumferential position of the pipe at 3.8 m ($L/D = 117$) from the inlet. The raw PLIF images were then binarized by a threshold approach and post-processed to remove entrained liquid and out-of-plane features.

Concerning the capacitance method, a sensor was arranged in the pipe at 4.3 m from the inlet ($L/D = 133$). It consisted of two 16 mm long electrodes placed with an angle of 100° on opposite sides of the probe. A transducer measures the capacitance between them, which provides a voltage between 0 V and 10 V. This method allows the acquisition of a time-dependent signal that can be post-processed into the time trace of

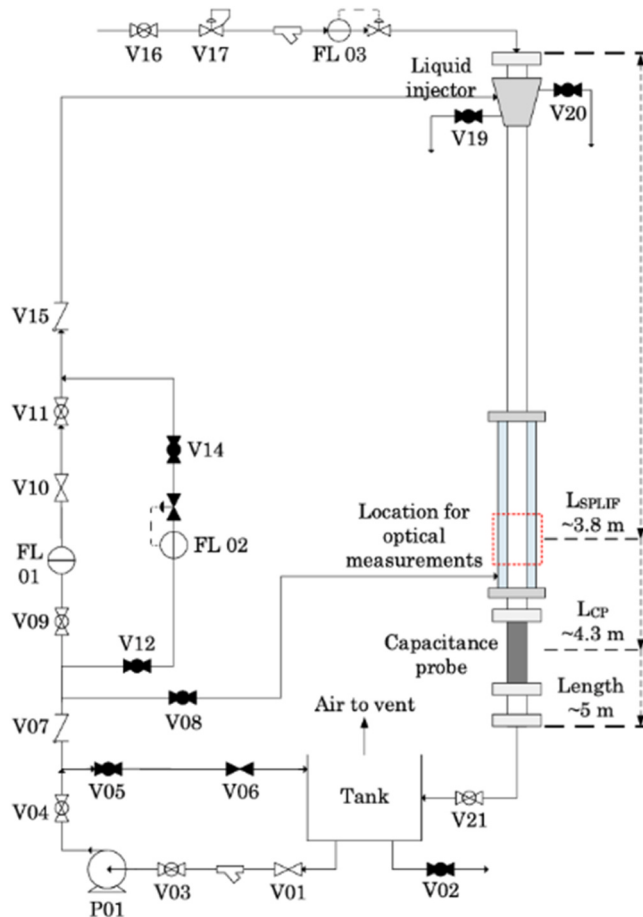


Fig. 3. Schematic of the experimental facility considered (Voulgaropoulos et al., 2021).

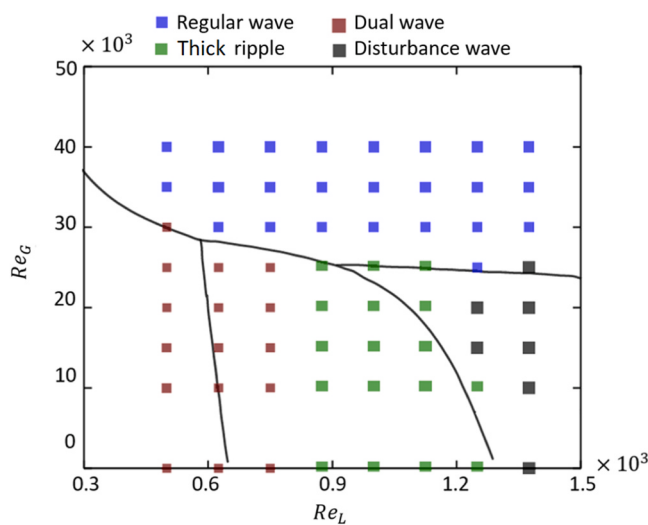


Fig. 4. Flow conditions investigated in the experimental campaign reported in Voulgaropoulos et al. (2021).

film thickness. The capacitance method measured the flow for 20 s, at a frequency of 10 kHz.

3. Numerical model

A CFD model has been developed and applied to a 2-D and 3-D

geometry. This section describes the governing equations, computational domain, numerical settings, and boundary conditions.

3.1. Governing equations

This study uses the VOF approach to model the two immiscible phases, air and water. In the VOF method, in addition to the conservation equations for mass and momentum, one solves an equation for the filled fraction of phase n in each control volume, α_n , so that $\alpha_n = 1$ in filled controlled volumes and $\alpha_n = 0$ in empty control volumes. From the continuity equation, one can show that the evolution of α_n is governed by the following transport equation:

$$\frac{\partial \alpha_n}{\partial t} + \nabla \cdot (\alpha_n \mathbf{v}) = 0 \quad (1)$$

In a two-phase system Eq. (1) is solved only for the second phase while the volume fraction of the first phase is computed given the constant of $\alpha_i + \alpha_j = 1$. The mixture density and viscosity are given by $\rho = \alpha_i \rho_i + (1 - \alpha_i) \rho_j$ and $\mu = \alpha_i \mu_i + (1 - \alpha_i) \mu_j$, respectively.

The equations for mass and momentum conservation can be written as:

$$\frac{\partial \rho}{\partial t} + \nabla \cdot (\rho \mathbf{v}) = 0 \quad (2)$$

$$\frac{\partial}{\partial t} (\rho \mathbf{v}) + \nabla \cdot (\rho \mathbf{v} \mathbf{v}) = -\nabla p + \nabla \cdot (\bar{\tau} + \bar{\tau}_t) + \rho g + \mathbf{F} \quad (3)$$

where \mathbf{F} is a source term accounting for the surface tension force that acts only in the region of interface, i.e., in partially filled cells, $\bar{\tau}$ is the molecular stress tensor, and $\bar{\tau}_t$ turbulent stress tensor (Reynolds stresses).

The continuous surface force (CSF) model proposed by Brackbill et al. (1992) is used to calculate the momentum source term accounting for the surface tension force. The model interprets surface tension as a continuous, three-dimensional effect across the interface. Considering two phases, the momentum source term is:

$$\mathbf{F} = \sigma_{ij} \frac{\rho k_i \nabla \alpha_i}{\frac{1}{2}(\rho_i + \rho_j)} \quad (4)$$

Where ρ is the mixture density, σ_{ij} is the surface tension coefficient, and k_i is the local surface curvature. Note that if only two phases are present in a cell, then $k_i = -k_j$ and $\nabla \alpha_i = -\nabla \alpha_j$.

The RNG $k-\epsilon$ model with enhanced wall functions was chosen to describe the effect of turbulence due to its accuracy for many applications regarding wall-bounded flows with and without pressure gradients (Shih et al., 1995).

To improve turbulence modelling near the gas-liquid interface, the ϵ -equation has been modified by adding a source term, $S_{\epsilon,i}$, to account for the wall-like damping of turbulence near the interface. The damping source term has been calculated following the approach proposed by Egorov (2004).

$$S_{\epsilon,i} = \frac{A_i \Delta n C_\mu \rho_i}{k_i} \left(\frac{6B\mu_i k_i}{\rho_i \Delta n^2} \right)^2 \quad (5)$$

Where A_i is the interfacial area density for phase i , Δn is the cell height normal to interface, C_μ is a model constant equal to 0.09, and k_i is the turbulent kinetic energy for phase i . Finally, B is the damping factor assumed to be equal to 10.

In this study the interfacial anti-diffusion treatment is used to suppress the numerical diffusion that may result from the volume fraction advection scheme. A negative diffusion source term is applied only in interfacial cells, modifying the volume fraction equation as follows:

$$\frac{\partial \alpha_n}{\partial t} + \nabla \cdot (\alpha_n \mathbf{v}) = -\nabla \cdot [\nu_e \alpha_n (1 - \alpha_n)] \quad (6)$$

Table 2

Computational times required for the 3-D and 2-D simulations of the 0.6 m pipe.

Case	Number of cores	Calculation time [days]
3D	40	60
2D	16	4

In Eq. (6) v_c is the compression velocity in the direction normal to the interface.

$$v_c = \gamma |\nu| \frac{\nabla \alpha_n}{|\nabla \alpha_n|} \quad (7)$$

Where γ is the compression factor varying between 0 and 1.

The explicit nature of the anti-diffusion treatment and the numerical sharpening of the resulting interface could affect the convergence rate. Nevertheless, numerical studies indicate that a γ value of 0.75 is typically appropriate in most scenarios, as it has a minimal impact on convergence while still maintaining reasonably sharp interfacial behaviour (Gupta et al., 2015).

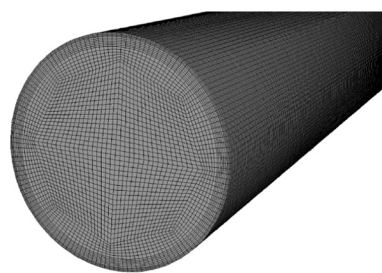
3.2. Domain and mesh

The experimental flow facility is a 5 m long vertical pipe of 32.4 mm in diameter (Voulgaropoulos et al., 2021)

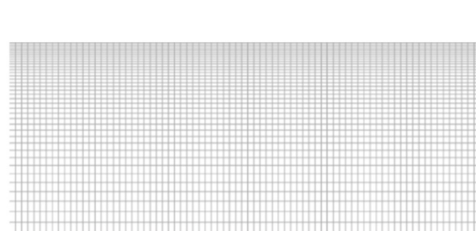
Since the VOF method requires a very fine mesh along the interface, the fully 3-D simulation of the entire pipe is not feasible with the available computer resources. Consequently, the section studied is 0.6 m long, reducing the computational time. Table 2 reports the computational times required by the 3-D and 2-D simulations.

The numerical study region begins at 0.35 m ($L/D = 11$), which is a good compromise between flow development and computational cost. Concerning the mean film thickness, the flow requires a higher axial length to develop (Wolf et al., 2001) than the one considered in this study. Nevertheless, the changes in the time-averaged film thickness with the axial dimension are generally small (Zhao et al., 2013), and the model can be validated directly against the experimental data. However, regarding waves activities, the flow continues to evolve throughout the entire length of the pipe and waves frequency undergoes an exponential decrease starting from the inlet (Cherdantsev et al., 2021). In the study of wave statistics performed in this work, the correlation from Cherdantsev et al. (2021) is applied to find the expected frequency at the same L/D of the experiments.

The 3-D geometry consists of a pipe of length 600 mm and diameter 32.4 mm; while the 2-D geometry is a plane of 600 mm \times 16.2 mm, as the flow is assumed to be axisymmetric (Fig. 5). For both of them, the size of the cells decreases towards the wall to capture the interface correctly. Aspect ratio and orthogonal quality have been checked during the mesh generation to ensure acceptable quality. In the experimental flow facility, air and water are introduced at the top of the pipe concurrently, and water is introduced as a film. To simulate these



(a) 3-D mesh.



(b) 2-D mesh.

Fig. 5. Details of the computational domain.

Table 3
Mesh characteristics.

Case	Number of cells	Maximum aspect ratio	Maximum skewness	Minimum orthogonal quality
2-D	54 000	5	0	1
3-D	4 320 000	7	0.48	0.72

Table 4
Summary of the simulation settings in ANSYS Fluent.

Criteria	Setting
Solver setup	Pressure based
Pressure-velocity coupling	PISO
Multiphase model	VOF explicit scheme. Implicit body-force formulation and sharp interface modelling with interfacial anti-diffusion. 2 phases: liquid primary, air: secondary, surface tension coefficient $\sigma_{GL} = 0.072 \text{ N m}^{-1}$
Surface tension model	Continuous surface force with wall adhesion, contact angle 120°
Turbulence model	RNG $k - \epsilon$ with turbulence damping $B = 10$ and default coefficients
Wall treatment	Enhanced wall functions
Operating conditions	Atmospheric pressure at the outlet, gravity in direction of the flow. Operating density = gas density
Pressure discretization	Modified body-force weighted
Surface tracking	Geo-reconstruction
Momentum, k, ϵ discretization	Second order upwind scheme
Transient formulation	First order implicit
Time step	Adaptive with $\text{CFL} < 0.75$ condition
Solution method	Non-iterative time advancement (NITA), conservative with instability detection
Under-relaxation factor	Default, given by NITA solver (optimized)

Therefore, the medium mesh has been used in the present study since it provides the best trade-off between accuracy and computational time. The 2-D mesh has been generated considering the same axial and radial cell size as the 3-D mesh. The mesh characteristics are presented in Table 3.

Both 2-D and 3-D geometries have an axial cell size of 0.5 mm, with inflation closer to the wall, being the nearest cell 0.1 mm long in the radial direction. The specified dimensions remain the same over the whole computational domain.

3.3. Solver setup and boundary conditions

The software ANSYS Fluent 2021 R1 was used for the simulations. Regarding solution methods, the VOF is solved by the explicit formulation, which renders a clear and crisp interface, allowing the use of the geo-reconstruction discretization scheme. The geo-reconstruction method preserves the volume fraction sharpness and boundedness ($\alpha = [0, 1]$).

The PISO algorithm is applied for the pressure-velocity coupling. The pressure scheme employed is the modified body-force weighted scheme, which is advised for problems that involve large body forces. It offers good convergence and robustness and is even more robust with the non-iterative time advancement (NITA) solver, which has been used in this study. All the numerical settings are collected in Table 4.

In the VOF formulation, the liquid is defined as the primary phase and the gas as secondary. The continuum surface force method is set with wall adhesion. The experimental pipe is made of fluorinated ethylene propylene (FEP), so a value of 120° was set for the contact angle between the pipe and the fluid (Guo, Helseth, 2015).

Inlet conditions are set as velocity inlets, with values obtained from the Reynolds numbers. Two cases are studied, gathered in Table 5. It should be noted that the liquid Reynolds number here provided refers to

Table 5
Cases studied in the CFD simulations.

Case	Re_G	Re_L	Flow regime
A	25 000	1 250	Regular wave
B	30 000	1 250	Regular wave

Table 6
Phases properties.

Phase	ρ [kg/m ³]	μ [kg/ms]	σ [Nm ⁻¹]
Air	1.185	1.84×10^{-5}	-
Water	997	8.94×10^{-4}	-
Air-water	-	-	0.072

the number calculated from the bulk-averaged velocity and mean film thickness, which cannot be properly calculated a-priori. However, for the geometry studied, it can be assumed to be four times smaller than the liquid Reynolds number based on the superficial liquid velocity and pipe diameter (Voulgaropoulos et al., 2021). The air inlet is set with $\alpha_G = 1$, while the water inlet $\alpha_G = 0$, so that liquid and gas are introduced separately. Atmospheric pressure outlet and wall non-slip shear condition are applied. For the 2-D case, an axisymmetric condition on the pipe axis is set.

Regarding turbulence boundary conditions, the turbulence intensity and hydraulic diameter are used to specify the turbulence parameters. Following the same approach as that used in Han, Gabriel, 2007, the liquid inlet is set to a low value of turbulent intensity because features of near-wall flow characterize the liquid film. It is set in both cases to 0.5%. The inlet turbulence intensity is set to 1%, and the same value, used only in the case of backflow, is considered at the outlet. The hydraulic diameter for the water inlet is 2 times the annular inlet length, i.e., 1 mm, while for the air inlet it is 31.4 mm. At the outlet the hydraulic diameter is equal to the diameter of the pipe.

Concerning the flow initialization, it was found that initializing with a water film does not improve the convergence rate, as the annular flow is not maintained, and a lot of very fast liquid entrainment is created, slowing down the simulation and bringing about instability. Consequently, the pipe is initialized full of air at the air velocity. An adaptive time step is used based on the Courant Friedrichs Lewy number (CFL) value, setting the maximum global Courant number to 0.75.

Finally, the flow is assumed to be adiabatic and incompressible. The phases properties are reported in Table 6.

4. Post-processing methods

Data from the numerical simulations are acquired after the initial transient, which ends when the volume averaged volume fraction reaches a stable value ($\pm 10\%$). The study region is set from 350 mm to 425 mm, where there is no outlet influence.

Once the flow is developed along the pipe, data acquisition begins along the study region. For each of the 3-D simulations, data was acquired over 0.65 s. Assuming the flow is not symmetric (this verification will be addressed later), measurements are made along 12 angular Section 2-D simulations assume the flow is identical in all the circumferential positions and the flow properties are measured over 4 s thanks to the lowered computational requirements. In this section, the post-processing of the local-scale data acquired from the numerical simulation is described. Firstly, the method to track the gas-liquid interface is presented, followed by the calculation of the film thickness and its time trace. Finally, the methods to calculate the wave statistics and the wave frequency at the length to diameter ratio considered are presented.

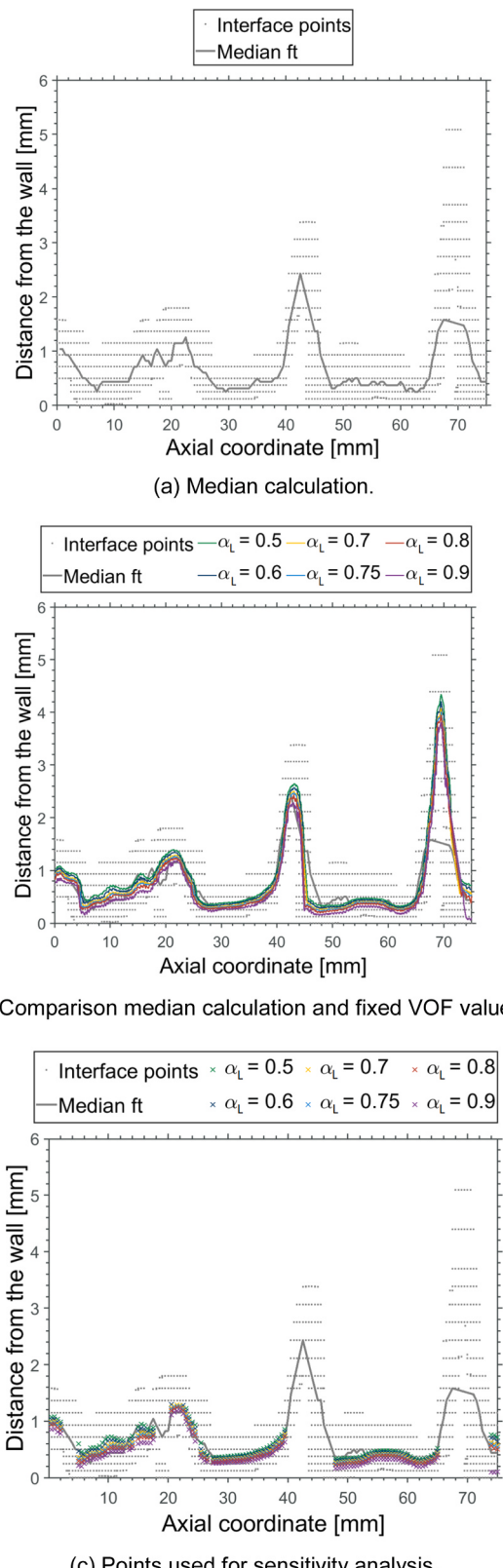


Fig. 7. Interface tracking: film thickness calculated as the median of interface points (a), issues found with the median calculation of film thickness (b), and sensitivity analysis performed to find the value of liquid volume fraction to track the interface.

4.1. Film thickness

Local film thickness can be calculated from the "height" of the film from the wall, i.e., from the radial coordinate of the interface points, at each axial coordinate: $h = R_{\text{pipe}} - R_{\text{interface}}$. In order to do that, it is necessary to track the interface. From the formulation of the VOF method, the volume fraction tracks the interface points. Theoretically, all the cell nodes with values between the numerical limits $0 < \alpha_l < 1$ are part of the interface. The film thickness can be calculated as the median of the height of these points $\delta(z) = \text{median}(h_i(z))$. However, several problems arise when film thickness is calculated in this way, as listed below:

- Fluent provides low axial and radial resolution when sampling so many points together, resulting in an irregular film thickness profile with missing data points.
- The median calculation becomes problematic and inaccurate when complex flow phenomena are present. For example, when the liquid film includes gas bubbles, or if the liquid is entrained into the core, it becomes quite complex to build a good filter that provides accurate results. Moreover, when waves are present, their crests are not appropriately captured, usually being underestimated due to the high density of points closer to the wall.

Some of the issues commented on previously can be seen in Fig. 7a. For example, the thickness of the larger waves is evidently underestimated. Besides, the gas entrainment that takes place at $z = 18\text{--}20$ mm is so close to the interface that it is not filtered properly, decreasing the value of film thickness when it should not.

For all of the above, it has been found that the interface can be better tracked by downloading the data from the points with a fixed value of the liquid volume fraction α_L . A sensitivity analysis is performed to find the specific value that best tracks the interface. Fig. 7b displays the film thickness obtained from different values of the volume fraction, calculated by the film thickness calculation algorithm that will be explained later on. As can be seen, another advantage of the proposed method is that the shape of the interface provided is smoother and more accurate in the whole domain.

The sensitivity analysis is based on the interface points that can be considered as non-problematic, i.e., the points where film thickness is accurately calculated as the median of the height of all the interface points. For the example studied, Fig. 7c marks the points used for the error calculation, which is performed as expressed in Eq. 8 for each α_i .

$$\text{error}_{\alpha_i} = \frac{|\delta^{\text{int}} - \delta^{\alpha_i}|}{\delta^{\text{int}}} \quad (8)$$

where δ^{int} is the film thickness calculated as the median of the eight of all the non-problematic interface points and δ^{α_i} is the film thickness obtained from a fixed value of the liquid volume fraction.

Values of α_L from 0.5 up to 0.9 were studied, calculating the spatial and time-averaged errors for the points considered. The results, presented in Table 7, indicate that the best interface tracking is obtained with a volume fraction of the liquid of 0.75 ± 0.25 . It should be noted that the minimum deviations correspond to $73 \mu\text{m}$ for Case A, and $80.8 \mu\text{m}$ for Case B. With the results from the sensitivity analysis, the acquisition of data for the calculation of film thickness is performed along the study region for the points with $\alpha_L = 0.75 \pm 0.25$.

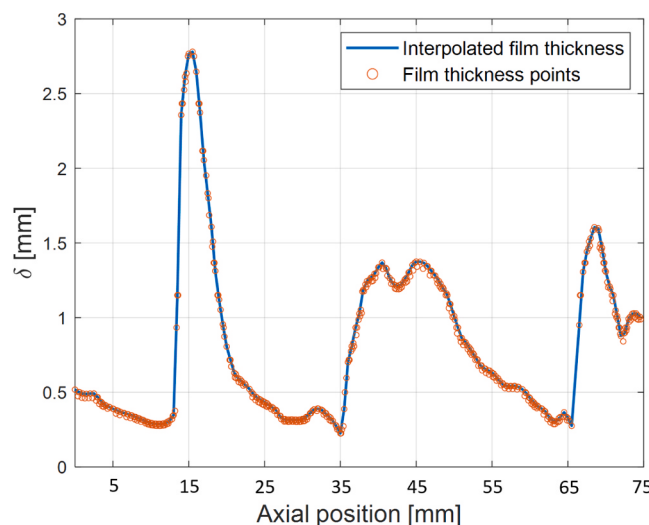
Once the interface is tracked, the main objective of the film thickness calculation is to obtain the time average (i.e., mean) film thickness $\langle \delta \rangle$. The standard deviation σ_δ is also computed, since it is useful to gain information on the wavy interface. In annular flow, the standard deviation is usually referred to as film roughness (Schubring et al., 2010).

The dataset acquired from the numerical simulations is formed by the radial coordinate of the points at the chosen α_L along the study region. For the 3-D case, the measurements are obtained at 12 circum-

Table 7

Sensitivity analysis of liquid volume fraction for interface tracking.

Case	Mean error $\alpha_L = 0.5$ [%]	Mean error $\alpha_L = 0.6$ [%]	Mean error $\alpha_L = 0.7$ [%]	Mean error $\alpha_L = 0.75$ [%]	Mean error $\alpha_L = 0.8$ [%]	Mean error $\alpha_L = 0.9$ [%]
A	22.0	17.0	14.2	13.9	14.5	19.7
B	21.9	15.4	15.2	14.9	20.8	19.7

**Fig. 8.** Film thickness over the study region.

ferential positions, every 30° . In this way, the local points of film thickness $\delta(z)$ can be calculated from the raw data at every time measurement and angle, (t_n, ϕ_p) , where $1 < n < N_t$ and $1 < p < N_p$. N_t is the total number of time measurements, and $N_p = 12$ for the 3-D case, $N_p = 1$ for the 2-D case. Once the height of the interface points is calculated, a process of filtering is applied.

The first filter sets the film thickness $\delta(z)$ as the maximum of the height $h(z)$, limiting this maximum by a value equal to 6 times the approximate mean film thickness ($\langle \delta_{\text{approx}} \rangle$). $\langle \delta \rangle_{\text{approx}}$ is a value updated in every calculation with the mean film thickness from all the previous calculations, approximating the final mean film thickness. The calculation from the maximum of the interface height can be done because α_L is a specific value, not the whole interface, and is helpful to eliminate most of the gas entrainment, along with some of the wave "under-cut". By limiting the maximum value, the most noticeable liquid entrainment is also deleted from the calculation.

After the first step, the film thickness obtained is filtered based on the expected value of $\delta(z)$, calculated through interpolation from its neighbours and thresholds that are dependent on $\langle \delta \rangle_{\text{approx}}$. The objective is to filter the outliers and more problematic mechanisms. This second process consists of a two-pass filtering, once in the axial direction, and then passing it again through the opposite direction. The thresholds

have been tuned for the case and should be chosen with care for each specific case.

To obtain the time trace of film thickness, the time evolution of film thickness is recorded focusing on a fixed axial position, at the middle point of the study region ($L/D = 12$). However, the local film thickness is not known at every axial position of the study region, since the axial and radial coordinates of the gas-liquid interface characterized by a liquid volume fraction of 0.75 are acquired. For this reason, the filtered discrete signal is interpolated to provide the required information. [Fig. 8](#) shows an example.

Given the time traces of film thickness also the time averaged (i.e., mean) film thickness $\langle \delta \rangle$ and the overall standard deviation σ_δ can be calculated.

The calculation of the film thickness and its evolution over time conforms to the first stage of the study of film thickness. The second stage consists of calculating the mean wave and base film thickness. In the experimental campaign of [Voulgaropoulos et al. \(2021\)](#), waves are defined as a disturbance of the liquid film interface over the film, which is characterized by $\langle \delta \rangle$. Therefore, the base film can be defined as the points of the film with $\delta_{\text{base}} \leq 2\langle \delta \rangle$, whereas the waves are considered points with $\delta_{\text{wave}} > 2\langle \delta \rangle$. The factor of 2 is chosen in the experimental approach from several sensitivity analyses performed in previous experiments. It is also used in the numerical simulations to provide comparable results. Mean base and wave film thickness are the temporal average of δ_{base} and δ_{wave} , respectively.

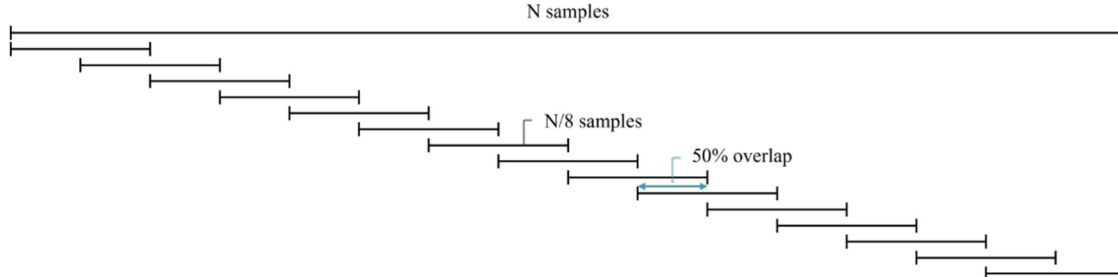
4.2. Wave statistics

The procedure explained in [Section 4.1](#) has been used to obtain a reliable representation of the film thickness time traces, which, in turn, have been used to calculate the corresponding power spectra.

The power spectrum of a non-linear signal can be estimated by the extensive use of the fast Fourier transform algorithm (FFT). This algorithm efficiently computes the discrete Fourier transform (DFT) of a finite length sequence with N points.

There are mainly two approaches, the first one is the analysis of the periodogram or power spectral density (PSD), which is based on applying directly the Fourier transform. The second approach is based on estimating first the autocovariance and then calculating the Fourier transform of that estimation. It should be noted that the analyses of these estimators are mostly approximate, so the most important qualitative results are studied here, as well as in the experiments. The first analysis is followed in this work.

The DFT of a signal provides good results in finding the spectrum of finite-duration signals and it is applied as shown in [Eq. \(9\)](#), where $X(k)$ is

**Fig. 9.** Segments and overlapping applied during the Welch estimation of the power spectral density.

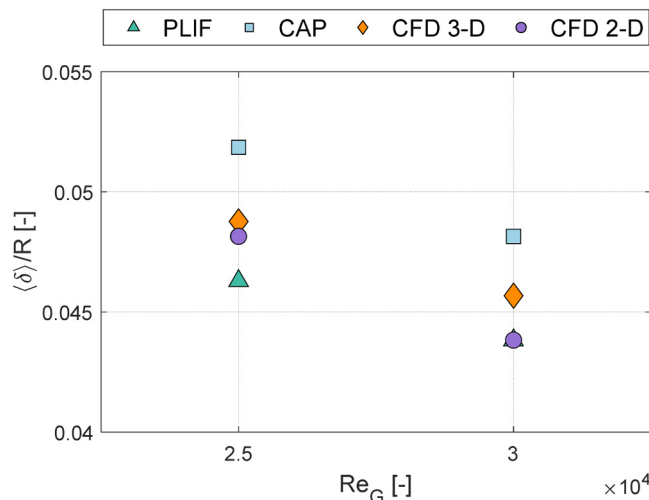


Fig. 10. Mean film-thickness as a function of the gas Reynolds number.

the discrete frequency spectrum of the time sequence $x(n)$.

$$X(k) = \sum_{n=0}^{N-1} x(n) e^{-j2\pi kn/N} \quad (9)$$

In order to find the spectrum of a signal, several steps are required beyond computing the DFT. First, the signal should be windowed in order to select a finite-length segment for a good estimation. In this case, the window applied is known as the Hamming window, which guarantees positive estimations and transforms the samples as follows:

$$\omega_H[\delta] = \begin{cases} 0.54 + 0.46\cos\left(\frac{\pi\delta}{M-1}\right) & |\delta| < M-1 \\ 0 & \text{otherwise} \end{cases} \quad (10)$$

The Hamming window allows the truncation of the signal to reduce excessive noise and smooth the output. Once the signal is windowed, the spectral density in the frequency spectrum is computed as

$$S_{xx}(k) = |X(k)|^2 \quad (11)$$

For the calculation of the PSD from the time trace, the Welch power spectral density estimate is computed, which applies a FFT algorithm for an efficient calculation. The total number of samples N is separated into windowed segments of length $N/8$ (Fig. 9). To apply the DFT to each of these segments, the discrete time-series needs to be extended with a proper number of zeros so that the total number of data points is a power of 2 (zero padding). The magnitude-squared of the DFT is then averaged by overlapping the segments at 50%, so that the variance of the noise spectrum is reduced. The signal also needs to be pretreated to remove trends (the mean film thickness), otherwise, the spectrum could be shifted due to the mean value, while the objective of the analysis is to study the wavy characteristics. Fig. 10.

Numerical measurements are performed at a lower L/D than in the experiments. Wave frequency and wavelength are still developing at the L/D considered in the numerical model. The main reason for this is a phenomenon known as wave coalescence. At the inlet of the pipe, interfacial waves are created due to the gas shear, and they have a specific velocity that is still developing due to the gravity and friction forces. Some waves may accelerate more than others, and with downstream distance, it is very common that several waves can merge and become one unique wave with a larger wavelength.

Several articles have been published on the evolution of disturbance waves. Cherdantsev et al. (2021) found that with downstream distance, the wave frequency in DAF decreases in an exponential manner, with an approximated function $f(x) = ae^{-bx} + c$, where $c = f_\infty$ is the presumed frequency at infinity (flow fully developed), $f_0 = a+c$ is the presumed

Table 8
Modal frequency for $L/D = 133$ and 12.

Case	f_{133} [Hz]	f_{12} [Hz]
A	12.0	30.4
B	13.6	35.9

Table 9
Mean film thickness and film roughness.

(a) Case A.				
	CAP	PLIF	CFD 3-D	CFD 2-D
$\langle \delta \rangle$ [mm]	0.84	0.75	0.79	0.78
σ_δ [mm]	0.64	0.73	0.57	0.68
$\langle \delta_{base} \rangle$ [mm]	0.63	0.55	0.63	0.58
$\langle \delta_{wave} \rangle$ [mm]	1.79	1.97	2.14	2.18
(b) Case B.				
	CAP	PLIF	CFD 3-D	CFD 2-D
$\langle \delta \rangle$ [mm]	0.78	0.71	0.74	0.71
σ_δ [mm]	0.55	0.63	0.51	0.6
$\langle \delta_{base} \rangle$ [mm]	0.6	0.53	0.61	0.54
$\langle \delta_{wave} \rangle$ [mm]	1.57	1.77	1.90	1.97

Table 10
Relative errors of the mean thickness and film roughness results.

(a) Case A.				
	CFD 3-D vs CAP	CFD 3-D vs PLIF	CFD 2-D vs CAP	CFD 2-D vs PLIF
$\text{err}_{\langle \delta \rangle}$ [%]	-6.2	+5.05	-6.77	+4.41
$\text{err}_{\sigma_\delta}$ [%]	-10.41	-21.46	+5.87	-7.18
$\text{err}_{\langle \delta_{base} \rangle}$ [%]	+0.05	+14.60	-8.33	+5
$\text{err}_{\langle \delta_{wave} \rangle}$ [%]	+19.66	+8.73	+21.60	+10.49
(b) Case B.				
	CFD 3-D vs CAP	CFD 3-D vs PLIF	CFD 2-D vs CAP	CFD 2-D vs PLIF
$\text{err}_{\langle \delta \rangle}$ [%]	-5.13	+4.23	-8.97	0
$\text{err}_{\sigma_\delta}$ [%]	-7.27	-19.05	+8.33	-5
$\text{err}_{\langle \delta_{base} \rangle}$ [%]	+1.67	+15.09	-10	+1.89
$\text{err}_{\langle \delta_{wave} \rangle}$ [%]	+21.02	+7.34	+25.48	+11.23

frequency at the inlet, a theoretical limit, and b is the exponential decrement. From the investigation, it is also found that the ratio f_0/f_∞ equals 3.

Assuming that the modal frequency from the experiments can be considered f_∞ the parameters a and c can be directly calculated. The exponential decrement b is calculated from the results in Cherdantsev et al. (2021) for similar gas and liquid Reynolds numbers. The experimental frequency and the calculated frequency for the numerical length are presented in Table 8. Apart from wave frequency, wave coalescence increases the maximum peak of the waves, but also its wavelength, as the liquid from two waves is now carried by one.

5. Results and discussion

In this section, the numerical results are presented and compared with the experimental data. First, mean film thickness, film roughness, and mean base and wave film thickness are considered. Second, wave statics are analyzed and commented.

5.1. Film thickness

The mean film thickness and film roughness are calculated for both

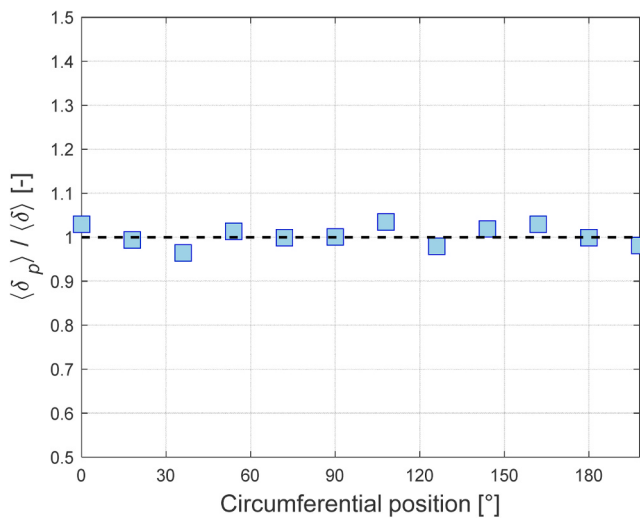


Fig. 11. Normalized mean film thickness as a function of the circumferential position. Case B.

cases and the results are presented in Table 9, where a direct comparison with the experimental results can be made. As seen in Section 2, film thickness results were obtained from two methods: capacitance probe (CAP) and optical method (PLIF). Table 10 shows the errors of the numerical results relative to both the experimental methods which are calculated as follows.

$$\text{err\%} = \frac{y_{\text{CFD}} - y_{\text{exp}}}{y_{\text{exp}}} \cdot 100 \quad (12)$$

Regarding the mean film thickness, both the 3-D model and 2-D model provide good results, with relative errors always less than 10%, indicating that the flow can be considered circumferential symmetric in terms of time-averaged flow properties. This statement is confirmed by Fig. 11, which shows the time-averaged film thickness for each circumferential positions, $\langle \delta_p \rangle$, normalized with the overall mean film

thickness, $\langle \delta \rangle$, considering Case B as an example.

The time-averaged normalized mean film thicknesses are randomly arranged around 1, with a standard deviation of 0.015 and 0.016 for Case A and Case B, respectively.

Nevertheless, as shown in Fig. 12, the flow is characterized by a strong instantaneous asymmetry, with circumferential localized waves with amplitude much larger than the mean film thickness. The waves shown in Fig. 12 cannot be classified as disturbance waves, which appear as coherent structures covering the entire pipe circumference with an amplitude 5–6 times the mean film thickness (Belt et al., 2010; Zhao et al., 2013). However, also non-coherent structures, similar to the ones shown in Fig. 12, named ephemeral wave, exist (Sekogushi and Takeishi, 1989; Wolf et al., 1996). The ephemeral waves are characterized by lower velocities than the disturbance waves, but they can exhibit identical dimensions to the disturbance waves.

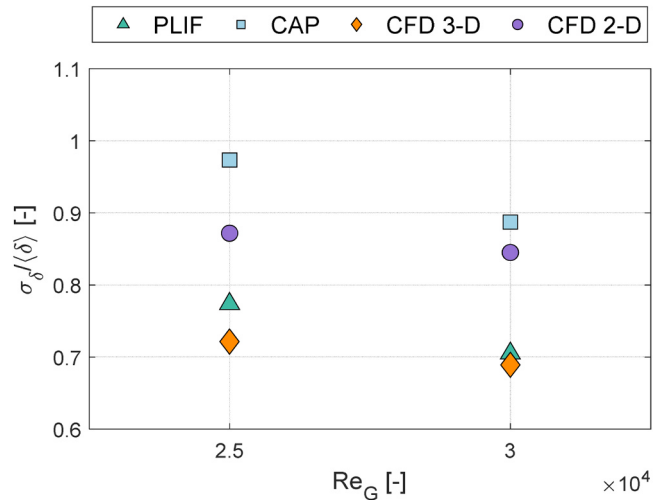


Fig. 13. Normalized film-roughness measurement as a function of gas Reynolds number.

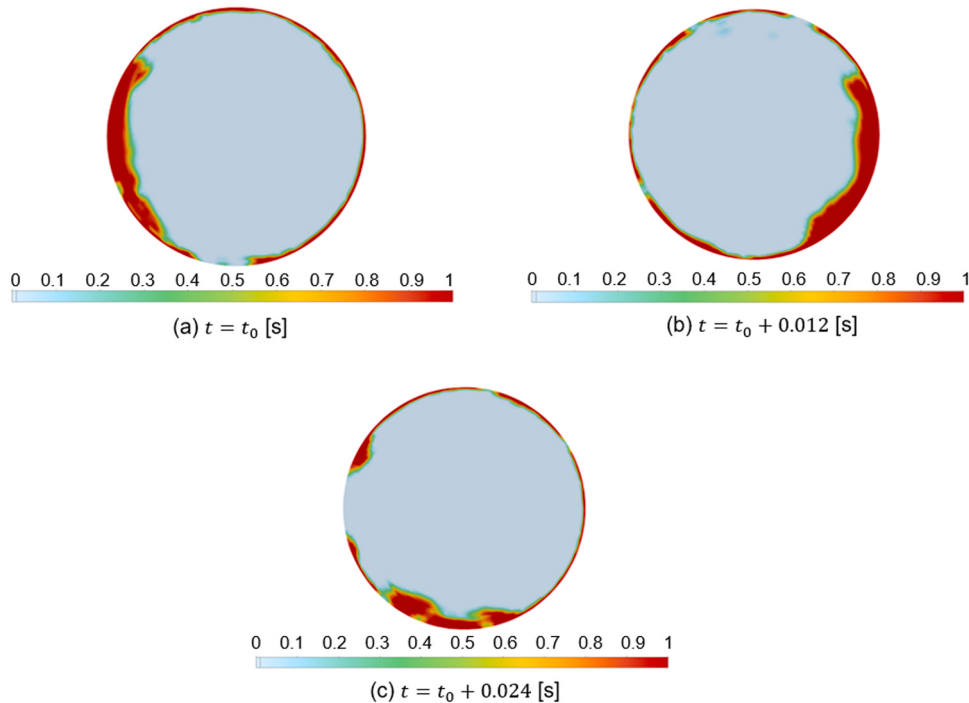
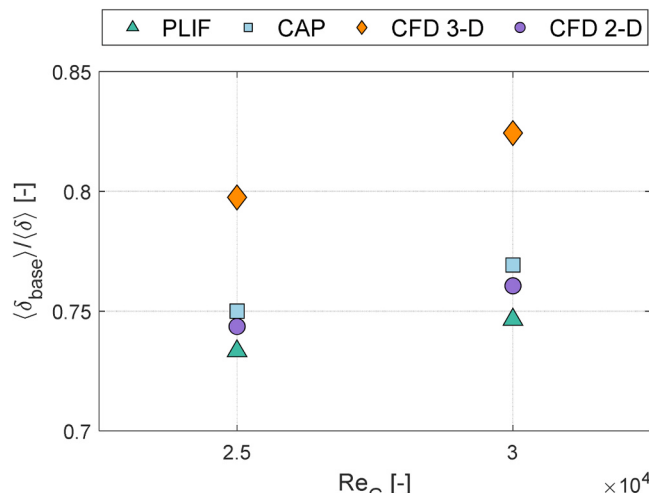
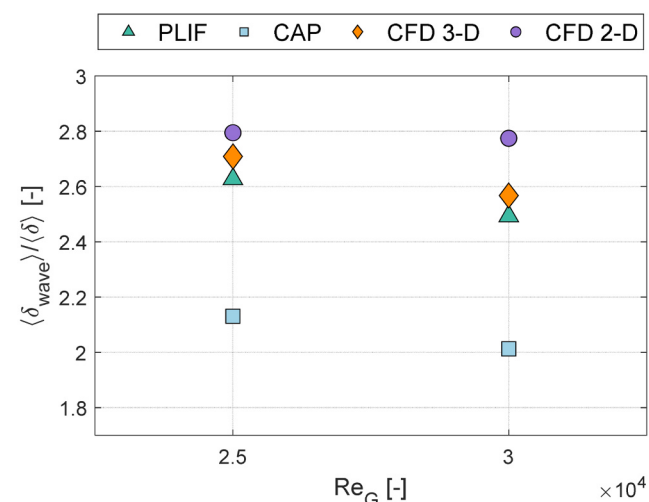


Fig. 12. Water volume fraction at different flow time over the cross section of the pipe. Case A.



(a) Relative mean base film thickness.



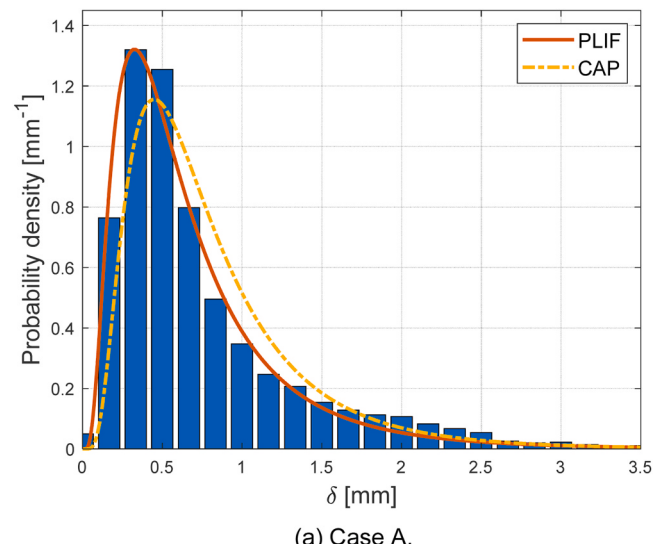
(b) Relative mean wave film thickness.

Fig. 14. Normalized mean base and wave film thickness.

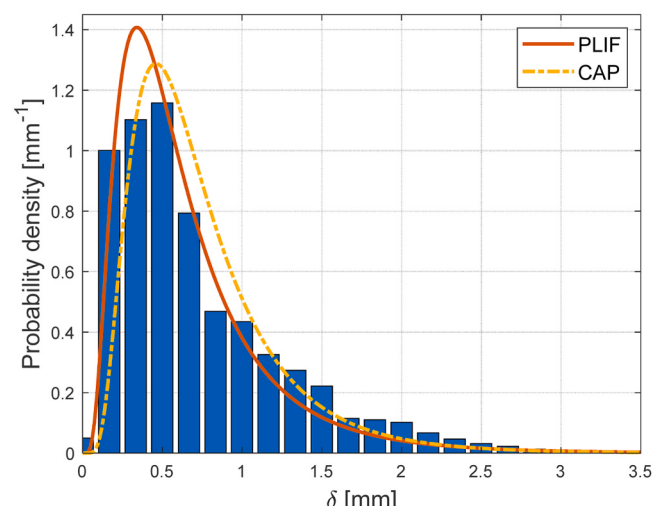
The modelling of large-amplitude waves is fundamental in annular flow since they govern the drop creation process, which strongly influences the pressure drop. For this reason, a 3-D modelling approach is needed, although 2-D simulations can provide good results in terms of time averaged flow properties.

The second moment of film thickness is evaluated in terms of relative film roughness, calculated as $\sigma_\delta/\langle\delta\rangle$ (Fig. 13). In the experiments, the gas shear does not impose a clear trend on the relative film roughness, which appears to increase at low gas Reynolds numbers and decrease when the gas Reynolds number is higher than 30,000. The influence of the gas Reynolds number over the relative film roughness cannot be analyzed in this study since only two conditions have been studied. Despite that, a comparison between numerical and experimental data can be performed. Fig. 13 shows that the numerical results agree with the experimental data, with the 3-D model better aligned with the PLIF measurements with respect to the CAP results.

On the contrary, if the film roughness is considered (not normalized with respect to the time averaged film thickness) (Table 9) the 3-D model results better agree with the CAP measurements and the 2-D results are better aligned with the PLIF findings. Indeed, the 3-D and 2-D approaches give the same time-averaged film thickness with a higher standard deviation for the 2-D model.



(a) Case A.



(b) Case B.

Fig. 15. Comparison between the probability density distributions obtained from the numerical results and the experimental PDFs. The numerical results refer to the 3-D simulations. The histograms are determined starting from the time-traces of film thickness for all the circumferential positions considered, without introducing spatial averaging.

As shown in Table 9, the 3-D model standard deviation is lower than the experimental one. This can be explained considering that for higher L/D than that analyzed in this study, wave coalescence takes place, and the longitudinal size of the waves increases, although mean film thickness is maintained, as well as the mean base and wave height. For this reason, it is expected that higher L/D waves present higher peaks and, hence, a slightly greater standard deviation.

Results for the mean wave and base film thickness are shown in Figs. 14a and 14b. The relationship between the thickness of the base film and that of the whole film in the numerical models is close to the experimental values, with a maximum relative error between numerical and PLIF results less than 10%.

5.2. Wave statistics

Fig. 15 shows the probability density distribution of the liquid film thickness calculated from the numerical results for Case A and Case B, considering the 3-D model.

The probability density distributions for film thickness are

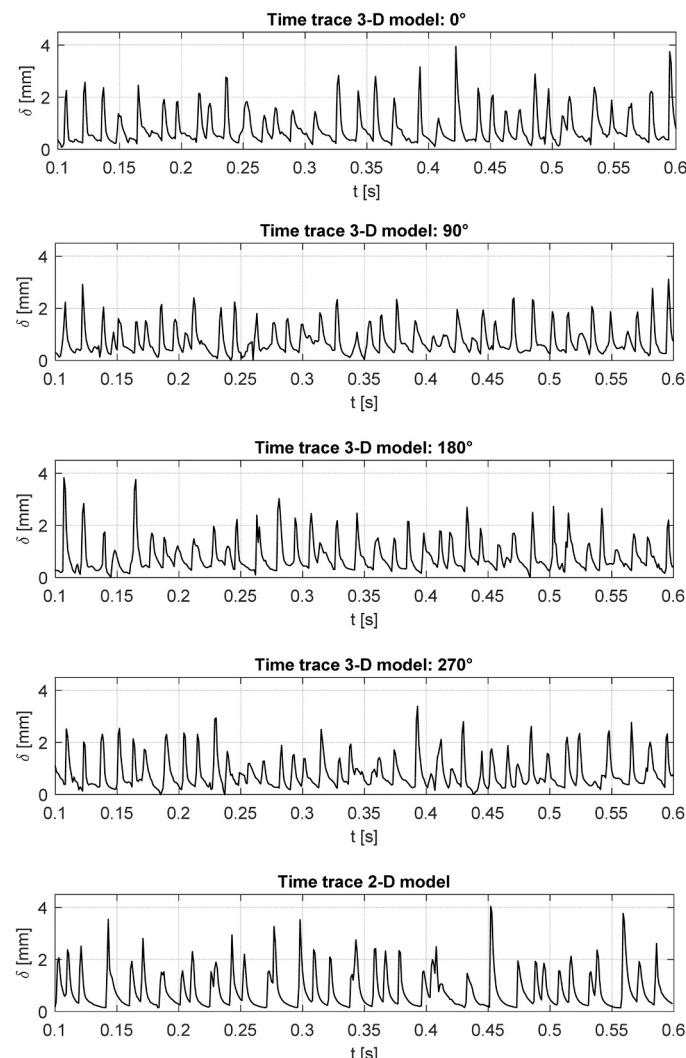


Fig. 16. Time traces of film thickness for Case B determined recording the time history of film thickness at $L/D = 12$. A filtering procedure has been applied to the raw data from the numerical simulations.

asymmetric and positively skewed, exhibiting a tail that extends towards greater film thickness values.

The Case A probability density distribution shows a dominant peak at low film thickness attributed to the base film in perfect agreement with the PLIF findings. On the contrary, the probability density distribution concerning Case B shows a trend that falls in between the PLIF and CAP findings, with a distribution peak better aligned with the CAP results.

Focusing on wave activities, the procedure explained in Section 4.1 has been used to represent the time evolution of film thickness, shown in Fig. 16 and Fig. 17 for Case A and Case B, respectively.

The 3-D time traces present typical characteristics of the regular wave regime, with waves of short wavelength and increased amplitude which are generated in a regular manner by the enhanced gas shear. Instead, the 2-D time traces appear closer to those of the disturbance wave regime, with irregular large-scale waves of shorter wavelength than those of the base film, carrying small scale ripples (Voulgaropoulos et al., 2021).

Considering the time trace at different circumferential positions and following the approach proposed by Zhao et al. (2013), the cross-correlation coefficients between them have been calculated to determine the presence of circumferential coherent waves. The results are presented in Table 11 and Table 12 for Case A and Case B,

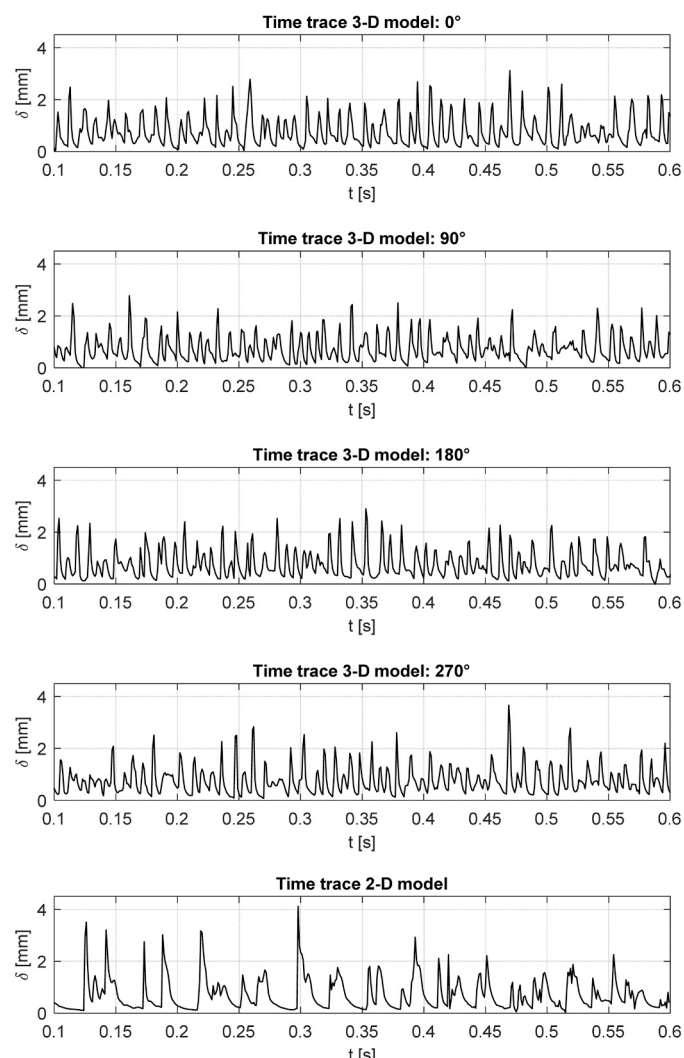


Fig. 17. Time traces of film thickness for Case B determined recording the time history of film thickness at $L/D = 12$. A filtering procedure has been applied to the raw data from the numerical simulations.

Table 11

Cross-correlation coefficients between 6 different circumferential positions. Case A.

	30°	90°	150°	210°	270°	330°
30°	1	0.70	0.64	0.65	0.65	0.68
90°	-	1	0.70	0.69	0.68	0.72
150°	-	-	1	0.75	0.66	0.67
210°	-	-	-	1	0.68	0.67
270°	-	-	-	-	1	0.70
330°	-	-	-	-	-	1

Table 12

Cross-correlation coefficients between 6 different circumferential positions. Case B.

	30°	90°	150°	210°	270°	330°
30°	1.00	0.64	0.68	0.65	0.61	0.70
90°	-	1.00	0.71	0.68	0.67	0.72
150°	-	-	1.00	0.70	0.65	0.72
210°	-	-	-	1.00	0.69	0.69
270°	-	-	-	-	1.00	0.72
330°	-	-	-	-	-	1.00

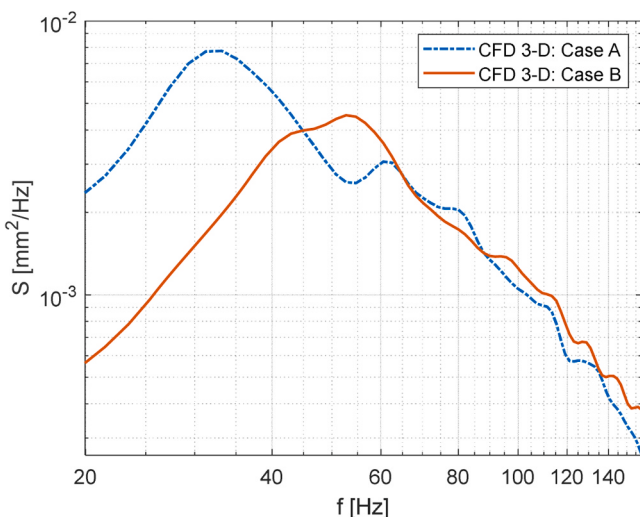


Fig. 18. Power spectra obtained from the film thickness time traces.

Table 13
Modal frequency results obtained from the PSD analysis.

Case	f_{EXP}	$f_{3\text{-}D}$	$f_{2\text{-}D}$	$\text{err}_{3\text{-}D} [\%]$	$\text{err}_{2\text{-}D} [\%]$
A	30.4	33.2	15.6	+ 9.21	-48.68
B	36.2	52.7	16.6	+ 45.58	-54.14

respectively.

The high value of the cross-correlation coefficients indicates the presence of coherent waves over the circumference of the pipe, following the results of Zhao et al. (2013). In addition, from the visual inspection of the time traces, it is possible to observe how these waves have a peak height not uniform over the circumferential perimeter of the pipe, supporting the findings of Hewitt and Lovegrove (1969).

To provide a deeper insight into waves activity, the power spectral density functions for Case A and B, have been generated starting from the time traces at the different circumferential positions. The results are shown in Fig. 18, concerning the 3-D model.

The functions have a global maximum at the modal frequency (Table 13), which is shifted at higher frequencies but at lower power for Case B (characterized by a higher gas Reynolds number) in agreement with the experimental results of Vougaropoulos et al. (2021). However, it must be pointed out that the difference in the modal frequency and power between Case A and Case B is largely overestimated by the numerical model.

The PSDs are characterized by a quasi-linear power decay, similar to that of the power-law decay of the Kolmogorov spectrum for homogeneous and isotropic turbulence, which becomes slightly steeper for Case A, characterized by a lower gas Reynolds number (PDF function slope of 2.15 and 1.87 for Case A and Case B, respectively). Indeed, an increase in the gas Reynolds number results in an energy introduction into the interfacial structure at progressively higher frequencies.

Concerning the 2-D model, the calculated modal frequencies differ completely from the experimental values. In particular, they are largely underestimated, reflecting the wrong trend of the time traces shown in Fig. 16 and Fig. 17, which are more similar to those of the disturbance wave regime rather than those of the regular wave regime.

6. Conclusions

This study proposed a CFD model for simulating the regular wave regime in downwards annular flows. A 3-D and 2-D models have been developed, and the results have been compared with available experimental data.

The 3-D and 2-D approaches provide similar results in terms of time-averaged flow properties. However, the 3-D model reveals that flow is characterised by a strong instantaneous asymmetry related to the presence of waves with large amplitude not coherent over the pipe circumference. Consequently, the axisymmetric condition is not applicable to the studied case. In addition, the wavy interface from the 2-D model presents larger waves at lower frequency than what is expected for the applied flow conditions.

On the other side, the analysis of the flow obtained by the 3-D approach was satisfactory. Mean film thickness is in good agreement with the experimental results, with a slightly lower standard deviation that might be due to the lower L/D than the one considered in the experiments.

The analysis of the time traces at different circumferential positions, reveals how waves are coherent over the circumferential perimeter of the pipe, in accordance with the experimental findings of Zhao et al. (2013).

Regarding the power spectral analysis, the PSDs functions from the 3-D model are characterised by a quasi-linear power decay with a higher modal frequency for Case B, characterised by a higher gas Reynolds number. This finding agrees with the experimental data of Zadrazil et al. (2014), though the numerical model largely overestimates the difference in the modal frequency between the two cases analysed. Conversely, the power spectral results from the 2-D model completely differ from the experimental results.

As a further development, the simulated operating conditions could be expanded by studying other gas and liquid Reynolds numbers and moving to other flow regimes. In addition, the post-processing procedure could be enhanced to characterize disturbance and ephemeral waves in terms of wave frequency and velocity.

Finally, a sensitivity analysis on the turbulence damping coefficient should be performed, to study its influence on wave activities.

Declaration of Competing Interest

The authors declare that they have no known competing financial interests or personal relationships that could have appeared to influence the work reported in this paper.

References

- Alekseenko, S.V., Antipin, V.A., Cherdantsev, A.V., Kharlamov, S.M., 2008. Investigation of waves interaction in annular gas-liquid flow using high-speed fluorescent visualization technique. Microgravity Sci. Technol. 20, 271–275.
- Angirekula, V.K.R., Gupta, R., 2022. A numerical study of wave characteristics in axisymmetric gas-liquid annular flow in microchannels. Chem. Eng. Res. Des. 182, 629–644.
- Belt, R.J., Van't Westende, J.M.C., Prasser, H.M., Portela, L.M., 2010. Time and spatially resolved measurements of interfacial waves in vertical annular flow. Int. J. Multiph. Flow. 36 (7), 570–587.
- Brackbill, J.U., Kothe, D.B., Zemach, C., 1992. A continuum method for modeling surface tension. J. Comput. Phys. (2), 335–354.
- Charogiannis, A., Sik An, J., Vougaropoulos, V., Markides, C.N., 2019. Structured planar laser-induced fluorescence (S-PLIF) for the accurate identification of interfaces in multiphase flows. Int. J. Multiph. Flow. 118, 193–204.
- Cherdantsev, M.V., Isaenkov, S.V., Cherdantsev, A.V., Markovich, D.M., 2021. Development and interaction of disturbance waves in downwards annular gas-liquid flow. Int. J. Multiph. Flow. 138, 103614.
- De Schepper, S.C.K., Heynderickx, G.J., Marim, G.B., 2008. CFD modelling of all gas-liquid and vapor-liquid flow regimes predicted by the Baker chart. Chem. Eng. J. 138, 349–357.
- Egorov, Y., 2004. Contact Condensation in Stratified Steam-Water Flow. EVOL-ECORDA-D 07.
- Fan, W., Li, H., Anglart, H., 2019. Numerical investigation of spatial and temporal structure of annular flow with disturbance waves. Int. J. Multiph. Flow. 110, 256–272.
- Fan, W., Cherdantsev, A.V., Anglart, H., 2020. Experimental and numerical study of formation and development of disturbance waves in annular gas-liquid flow. Energy 207, 118309.
- Ghosh, S., Das, G., Das, P.K., 2010. Simulation of core annular downflow through CFD - a comprehensive study. Chem. Eng. Process 49, 1222–1228.

- Guo, X.D., Helseth, L.E., 2015. Optical and wetting properties of nanostructured fluorinated ethylene propylene changed by mechanical deformation and its application in triboelectric nanogenerators. *Mater. Res. Express* 2, 015302.
- Gupta, V.K., Khan M., Punekar, H., 2015. Development and Application of Interfacial Anti-Diffusion and Poor Mesh Numerics treatment for Free Surface Flows. *IEEE 22nd International Conference on High Performance Computing Workshops*, Bengaluru, India.
- Han, H., Gabriel, K., 2006. Flow physics of upward cocurrent gas-liquid annular flow in a vertical small diameter tube. *Microgravity Sci. Technol.* 18, 27–36.
- Han, H., Gabriel, K., 2007. A numerical study of entrainment mechanism in axisymmetric annular gas-liquid flow. *J. Fluids Eng.* 129, 293–301.
- Hewitt, G.F. and Lovegrove, P.C., 1969 Frequency and velocity measurements of disturbance waves in annular two-phase flow. UKAEA Report AERE R4304.
- Jayanti, S., Hewitt, G.F., 1997. Hydrodynamics and heat transfer in wavy annular gas-liquid flow: a computational fluid dynamics study. *Int. J. Heat. Mass Transf.* 40, 2445–2460.
- Liu, A., Yan, C., Zhu, F., Gu, H., Going, S., 2021. Liquid film thickness of vertical upward annular flow in narrow rectangular channel. *Chem. Eng. Res. Des.* 175, 10–24.
- Li, Y., Li, W.Z., Quan, S.L., 2011. A self-standing two-fluid CFD model for vertical upward two-phase annular flow. *Nucl. Eng. Des.* 241, 1636–1642.
- Pinilla, A., Guerrero, E., Henao, D.H., Reyes, D.V., Pereyra, E., Soto, G., Ratkovich, N., 2019. CFD modelling of two-phase gas-liquid annular flow in terms of void fraction for vertical down- and up-ward flow. *SN Appl. Sci.* 1, 1–15.
- Riviera, Y., Muñoz-Cobo, J.L., Escrivá, A., Berna, C., Córdova, Y., 2022. Experimental measurements and CFD results of liquid film thickness in vertical downward air-water annular flow. *Int. J. Comput. Methods Exp. Meas.* 10, 93–103.
- Schubring, D., Ashwood, A.C., Shedd, T.A., Hurlburt, E.T., 2010. Planar laser-induced fluorescence (PLIF) measurements of liquid film thickness in annular flow. Part I: methods and data. *Int. J. Multiph. Flow.* 36, 815–824.
- Sekogushi, K., Takeishi, M., 1989. Interfacial structures in upward huge wave flow and annular flow regimes. *Int. J. Multiph. Flow.* 15 (3), 295–305.
- Shih, T.H., Liou, W.W., Shabbir, A., Yang, Z., Zhu, J., 1995. A new $k-\epsilon$ eddy viscosity model for high reynolds number turbulent flows. *Comput. Fluids* 24, 227–238.
- Voulgaropoulos, V., Patapas, A., Lecompte, S., Charogginnis, A., Matar, O.K., De Paep, M., Markides, C.N., 2021. Simultaneous laser-induced fluorescence and capacitance probe measurement od downwards annular gas-liquid flows. *Int. J. Multiph. Flow.* 142, 103665.
- Webb, D.R., Hewitt, G.F., 1975. Downwards co-current annular flow. *Int. J. Multiph. Flow.* 2, 35–49.
- Wolf, A., Jayanti, S., Hewitt, G.F., 1996. On the nature of ephemeral waves in vertical annular flow. *Int. J. Multiph. Flow.* 22 (2), 325–333.
- Wolf, A., Jayanti, S., Hewitt, G.F., 2001. Flow development in vertical annular flow. *Chem. Eng. Sci.* 56, 3221–3235.
- Wu, B., Firouzi, M., Mitchell, T., Rufford, T.E., Leonardi, C., Towler, B., 2017. A critical review of flow maps for gas-liquid flows in vertical pipes and annuli. *J. Chem. Eng.* 326, 350–377.
- Wu, J., Jiang, W., Liu, Y., He, Y., Chen, J., Qiao, L., Wang, T., 2020. Study on hydrodynamic characteristics of oil-water annular flow in 90° elbow. *Chem. Eng. Res. Des.* 153, 443–451.
- Xue, Y., Stewart, C., Kelly, D., Cambell, D., Gormley, M., 2022. Two-phase annular flow in vertical pipes: a critical review of current research techniques and progress. *Water* 14, 3496.
- Zabaraz, G., Dukler, A.E., Moalem-Maron, D., 1986. Vertical upward cocurrent gas-liquid annular flow. *AICHE J.* 32, 829–843.
- Zadrazil, I., Matar, O.K., Markides, C.N., 2014. An experimental characterization of downwards gas-liquid annular flow by laser-induced fluorescence: Flow regimes and film statistics. *Int. J. Multiph. Flow.* 60, 87–102.
- Zhao, Y., Markides, C.N., Matar, O.K., Hewitt, G.F., 2013. Disturbance wave development in two-phase gas-liquid upward vertical annular flow. *Int. J. Multiph. Flow.* 55, 111–129.
- Zhu, F., Yan, C., Liu, A., Gu, H., Gong, S., 2021. Droplet size of vertically upward annular flow in a narrow rectangular channel. *Chem. Eng. Res. Des.* 174, 107–115.